Nanoscale

PAPER

View Article Online
View Journal | View Issue

Cite this: *Nanoscale*, 2023, **15**, 1595

Second-order nonlinear optical properties of copper-based hybrid organic–inorganic perovskites induced by chiral amines†

Bin Li, ‡[a] Ying Yu,‡[a] Mingyang Xin,[b] Jialiang Xu, [b] Tianzhe Zhao,[a] Huimin Kang,[a] Guoxiang Xing,[a] Peisheng Zhao,[a] Tianyong Zhang*[a] and Shuang Jiang *[a]

Received 13th September 2022,
Accepted 2nd December 2022

DOI: 10.1039/d2nr05022f

rsc.li/nanoscale

Recently, chiral hybrid organic–inorganic perovskites (HOIPs) are drawing wide attention due to their intrinsic noncentrosymmetric structures which result in fascinating properties such as ferroelectronics and second-order nonlinear optics (NLO). However, previous research mainly focused on chiral lead-based halide perovskites ignoring that the toxic Pb element is harmful to humans and the environment. Herein, we successfully synthesized block-like (*R*-/*S*-NEA)$_2$CuCl$_4$ (NEA = 1-naphthylethylamine) and needle-like (*R*-/*S*-CYHEA)$_6$Cu$_3$Cl$_{12}$ (CYHEA = 1-cyclohexylethylamine) single crystals, which crystallize in the Sohncke $P2_1$ and $I2$ space group, respectively. Each pair of chiral perovskite enantiomers shows mirror circular dichroism (CD) signals. The thin films show an efficient second harmonic generation (SHG) response and the NLO coefficients of (*R*-NEA)$_2$CuCl$_4$ and (*R*-CYHEA)$_6$Cu$_3$Cl$_{12}$ are 11.74 and 3.04 pm V^{-1}, respectively, under 920 nm excitation with Y-cut quartz as a reference, which shows that the chiral amine has a significant effect on the SHG behavior. The high SHG response of (*R*-NEA)$_2$CuCl$_4$ is perhaps due to the rigidity of the aromatic amine, which leads to highly asymmetrical space groups. Our results provide guidelines for designing and tuning the SHG response in chiral HOIPs.

Introduction

Nonlinear optical (NLO) properties refer to the nonlinear interaction between light and matter that involves energy conversion of photons with different frequencies.[1] Second harmonic generation (SHG) is a process where two photons of frequency ω are annihilated with the simultaneous creation of a new photon with frequency 2ω.[2] When light with a certain wavelength interacts with SHG-active materials, the frequency of the generated emergent light will be twice that of the incoming light.[3] SHG-active materials as a key component of solid-state lasers show great potential in information encryption and clinical operations.[4–6] Many chiral hybrid organic–inorganic perovskites (HOIPs) possess non-centrosymmetric structures and have become SHG-active candidates. It is necessary for SHG properties that the materials have a noncentrosymmetric geometry. Therefore, molecular materials with noncentrosymmetry have been developed for SHG research.[2]

Chiral halide perovskites first came into people's view when Billing and Lemmerer first synthesized [(*S*)-$C_6H_5C_2H_4NH_3$][$PbBr_3$] in 2003.[7] Chiral HOIPs, which introduce chiral amines as site A to perovskite systems, possess air stability,[8] tunable optical properties,[9,10] symmetric circular dichroism (CD) signals,[11] the photovoltaic effect[12,13] and other chirality-related optoelectronic properties, thus creating a promising platform for chiral optoelectronics.[14] Owing to these excellent intrinsic characteristics, chiral HOIPs are theoretically and experimentally investigated in circularly polarized light (CPL) detection,[15–19] CPL emitting sources,[20,21] spintronics,[22–24] optoelectronic switches,[25] the NLO effect[26–30] and so on.[31] HOIPs offer great opportunities to tune the structure and electronic bandgap by changing the components. In addition to the low cost and processability, the third- and higher-order NLO properties of HOIPs have been extensively studied and used in optical devices. However, the second-order NLO effect is required for optoelectric devices and the frequency multiplication effect. The introduction of chiral amines to HOIPs breaks the centrosymmetric structure of chiral HOIPs, endowing chiral HOIPs with second-order NLO activity. For example, Xu *et al.* reported that the 1D

[a]*Tianjin Key Laboratory of Applied Catalysis Science and Technology, School of Chemical Engineering and Technology, Tianjin University, No. 135, Yaguan Road, Tianjin 300350, P. R. China. E-mail: tyzhang@tju.edu.cn, shuangjiang@tju.edu.cn*
[b]*School of Materials Science and Engineering, National Institute for Advanced Materials, Nankai University, Tongyan Road 38, Tianjin, 300350, P.R. China*

†Electronic supplementary information (ESI) available. CCDC 2206252, 2206261, 2206265 and 2206266. For ESI and crystallographic data in CIF or other electronic format see DOI: https://doi.org/10.1039/d2nr05022f

‡These authors contributed equally to this work.

chiral perovskite (*R*-/*S*-MPEA)$_{1.5}$PbBr$_{3.5}$(DMSO)$_{0.5}$ (MPEA = β-methylphenethylamine) shows NLO properties with the NLO coefficient of 0.68 pm V^{-1} at 850 nm.[26] Luo and co-workers studied the SHG activity of [(*R*/*S*)-3-aminopiperidine]PbI$_4$ single crystals,[32] and Wu's group reported that an effective SHG signal could be detected in [(*R*/*S*)-1-(4-chlorophenyl)ethylamine]$_2$PbI$_4$ single-crystalline microwire arrays.[30] However, the toxic Pb element seriously limits their further practical applications due to the biological and environmental hazards. Therefore, it means a lot to develop lead-free chiral HOIP materials.

In recent years, many researchers have focused on organic–inorganic Cu-based perovskites due to their multiform optical, magnetic and thermal properties. Mande *et al.* studied the thermochromic behavior of [(naphthylethylammonium)$_2$CuCl$_4$].[33] Zhang *et al.* prepared chiral 2D perovskite ferromagnets and revealed that their saturation magnetization is up to 12.5 emu g^{-1}.[34] He *et al.* reported the SHG-CD effect of 0D hybrid copper halides and the anisotropy factor is up to 0.41.[35] Herein, we prepared two pairs of copper based chiral HOIP enantiomers, (*R*-/*S*-NEA)$_2$CuCl$_4$ and (*R*-/*S*-CYHEA)$_6$Cu$_3$Cl$_{12}$ bulk single crystals. The size of (*R*-/*S*-NEA)$_2$CuCl$_4$ is about 14 × 9 × 5 mm, and that of (*R*-/*S*-CYHEA)$_6$Cu$_3$Cl$_{12}$ is about 10 × 1 × 1 mm (Fig. S1a and b†). The thin films prepared from single crystals showed high CD signals with the highest $|g_{CD}|$ of (*S*-NEA)$_2$CuCl$_4$ of 0.0284. It has been proven that the halogen in the HOIP has a great effect on its space group, resulting in different SHG responses.[36] In this work, we investigated the roles of amines on the NLO properties of chiral HOIPs. An obvious SHG response has been detected in (*R*-NEA)$_2$CuCl$_4$ and (*R*-CYHEA)$_6$Cu$_3$Cl$_{12}$ thin films. The second-order NLO coefficient of the (*R*-NEA)$_2$CuCl$_4$ thin film is approximately 4 times as large as that of the (*R*-CYHEA)$_6$Cu$_3$Cl$_{12}$ thin film, which might be attributed to the different electron conjugation structures caused by amines. We speculate that the naphthalene ring of the NEA molecule is a planar conjugated structure with rigidity, leading to a high degree of spatial asymmetry of (*R*-NEA)$_2$CuCl$_4$. Conversely, the CYHEA molecule has flexible boat and chair conformations, and it may switch between these two conformations during spin-coating, leading to a decrease in steric asymmetry. This work provides a new path to design perovskite materials with second-order NLO activity.

Shuang Jiang

Prof. Shuang Jiang received her Ph.D. degree from the School of Chemical Engineering and Technology at Tianjin University in 2017. She joined Prof. Kotov's group as a visiting student from November 2014 to November 2016. She worked as an assistant professor in the School of Chemical Engineering and Technology of Tianjin University from 2017. Her research focuses on the fabrication and property regulation of chiral inorganic nanomaterials, the second-order nonlinear optical properties and circularly polarized light emission of chiral perovskite nanomaterials and applications in optoelectronic devices.

Experimental

Materials

Copper chloride dihydrate (CuCl$_2$·2H$_2$O, 99%) was purchased from Heins Opde Technology Ltd (Tianjin, China). (*R*)-(+)-α-Naphthylethylamine (*R*-NEA, 98%, ee 96%) and (*S*)-(−)-α-naphthylethylamine (*S*-NEA, 98%, ee 98%) were purchased from Meryer Reagent Ltd (Shanghai, China). (*R*)-(+)-α-Cyclohexylethylamine (*R*-CYHEA, 98%, ee 96%) and (*S*)-(−)-α-cyclohexylethylamine (*S*-CYHEA, 98%, ee 98%) were purchased from Shanghai Xianding Biotechnology Co. Ltd (Shanghai, China). *N*,*N*-Dimethylformamide (DMF, 99.9%) was purchased from Aladdin Reagent Ltd (Shanghai, China). 48% aqueous hydrochloric acid (HCl), methanol (AR), ethanol (AR) and acetonitrile were purchased from Tianjin Real & Lead Chemical Co, Ltd, China. All of the reagents were used as received without further purification.

Synthesis of naphthylethylamine chloride (NEA:Cl)

Briefly, 5 mL of naphthylethylamine (*R*-/*S*-NEA) and 20 mL of ethanol were added to a 100 mL round-bottom flask. The mixture was stirred at 0 °C in an ice-water bath. 4 mL of HCl (37 wt% in water) was then added to the mixture dropwise and stirred for 4 h. Subsequently, the solvent was subjected to rotary evaporation at 70 °C. The remaining powder was dissolved in ethanol and then recrystallized in diethyl ether, and the process was repeated until a white NEA:Cl precipitate was formed. Finally, the product was dried at 60 °C under vacuum overnight.

Synthesis of cyclohexylethylamine chloride (CYHEA:Cl)

The synthesis of CYHEA:Cl is similar to that of NEA:Cl. Briefly, 5 mL of cyclohexylethylamine (*R*-/*S*-CYHEA) and 20 mL of ethanol were added to a 100 mL round-bottom flask. The mixture was stirred at 0 °C in an ice-water bath. 2.5 mL of HCl (37 wt% in water) was then added to the mixture dropwise and stirred for 4 h. Subsequently, the solvent was subjected to rotary evaporation at 70 °C. The powder was dissolved in ethanol and then recrystallized in diethyl ether, and the process was repeated until a white CYHEA:Cl precipitate was formed. Finally, the product was dried at 60 °C under vacuum overnight.

Synthesis of (*R*-/*S*-NEA)$_2$CuCl$_4$ single crystals

First, 1.71 g of CuCl$_2$·2H$_2$O (15 mmol), 4.15 g of NEA:Cl (20 mmol), and 15 mL of methanol were loaded in a glass vial. The mixture was stirred until all solids were dissolved, yielding a clear dark green solution. Then, 30 mL of acetonitrile was slowly added to the solution, forming an acetonitrile–metha-

nol diffusion layer. The solvent was allowed to slowly evaporate for two weeks and yellow block-like crystals (NEA_2CuCl_4) were grown out of the solution. The crystals were isolated by filtration, washed with an acetonitrile–methanol mixed solvent and dried in air.

Synthesis of (*R*-/*S*-CYHEA)$_6Cu_3Cl_{12}$ single crystals

First, 1.71 g of $CuCl_2{\cdot}2H_2O$ (15 mmol), 3.15 g of CYHEACl (20 mmol), and 15 mL of methanol were loaded in a glass vial. The mixture was stirred until all solids were dissolved, yielding a clear dark green solution. Then, 30 mL of acetonitrile was slowly added to the solution, forming an acetonitrile–methanol diffusion layer. The solvent was allowed to slowly evaporate for two weeks and brown needle-like crystals ($CYHEA_6Cu_3Cl_{12}$) were grown out of the solution. The crystals were isolated by filtration, washed with an acetonitrile–methanol mixed solvent and dried in air.

Preparation of thin films

The quartz substrates (2 × 2 cm^2) were cleaned with acetone, ethanol and deionized water in a sonicator for 10 min, respectively, followed by a plasma cleaner with oxygen plasma for 10 min to improve wettability. The precursor solutions were prepared by dissolving the corresponding single crystals in DMF with a concentration of 40 wt%. Thin films were prepared by spin-coating of the precursor on substrates at a spin rate of 2000 rpm for 30 s and evaporating the solvent at room temperature. Thin films on quartz substrates were used for optical (UV-vis absorption, CD and SHG) measurements. Thin films fabricated under the same conditions but on silicon wafers were used for XRD and refractive index measurements.

Results and discussion

The bulk single crystals of (*R*-/*S*-NEA)$_2CuCl_4$ and (*R*-/*S*-CYHEA)$_6Cu_3Cl_{12}$ were prepared through the slow solvent evaporation method at room temperature. The crystal structures (Fig. 1a and b) were characterized by single crystal X-ray diffraction (SCXRD) and crystal structure data are listed in Tables S1 and S2.† As shown in Fig. 1a, each (*R*-NEA)$_2CuCl_4$ molecule is made up of one isolated $[CuCl_4]^{2-}$ and two protonated *R*-NEA^+ cations. They crystallize in the monoclinic system with a Sohncke space group of $P2_1$. Two *R*-NEA^+ cations are coordinated with an irregular $[CuCl_4]^{2-}$ tetrahedron *via* the hydrogen bonds of N–H···Cl. The bond lengths of Cu–Cl vary from 2.2380 Å to 2.2592 Å. The powder X-ray diffraction (PXRD) patterns of (*R*-/*S*-NEA)$_2CuCl_4$ single crystals match well with the simulation results (Fig. 1c). What's more, the sharp diffraction peaks of the PXRD patterns indicate that the crystals have good crystallinity. (*R*-CYHEA)$_6Cu_3Cl_{12}$ crystallizes in the Sohncke *I*2 space group. Each (*R*-CYHEA)$_6Cu_3Cl_{12}$ molecule is made up of six $CYHEA^+$ cations, one $[Cu_3Cl_{10}]^{4-}$ and two isolated Cl^- anions (Fig. 1b). The bond lengths of Cu–Cl vary from 2.246 Å to 2.748 Å (Fig. S2†). The large variation in the Cu–Cl bond length can be traced back to the highly distorted

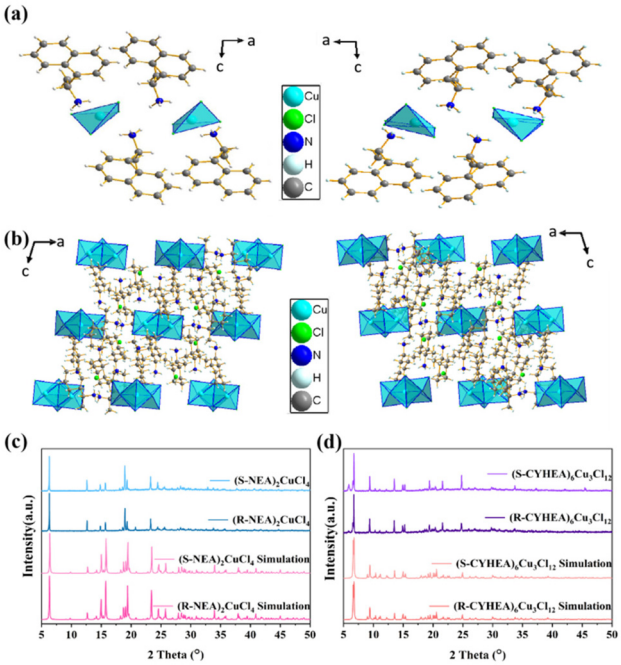

Fig. 1 The crystal structure of (a) (*R*-/*S*-NEA)$_2CuCl_4$ and (b) (*R*-/*S*-CYHEA)$_6Cu_3Cl_{12}$. PXRD patterns of (c) (*R*-/*S*-NEA)$_2CuCl_4$ and (d) (*R*-/*S*-CYHEA)$_6Cu_3Cl_{12}$ single crystals and the simulated results of single crystals.

$[Cu_3Cl_{10}]^{4-}$, which consists of three connected copper halide polyhedra. Like Cl2 and Cl4, they are connected to two Cu atoms, respectively. Therefore, a large variation in the Cu–Cl bond length is needed to maintain the stability of $[Cu_3Cl_{10}]^{4-}$. As shown in the PXRD images (Fig. 1c and d and the zoomed-in region in Fig. S3†), the *R*- and *S*-perovskite enantiomers share a similar structure, and the diffraction peaks match well with the simulation results of single crystals. For practical application, the stability of chiral perovskites in air is critical. The XRD patterns of (*R*-/*S*-NEA)$_2CuCl_4$ and (*R*-/*S*-CYHEA)$_6Cu_3Cl_{12}$ bulk single crystals show no change after exposure to air for 6 months (Fig. S4†), demonstrating their excellent stability.

To further confirm the identity of the organic molecule in the crystals, Fourier transform infrared (FTIR) spectra were recorded and are shown in Fig. S5.† The wide peak at 3250–2850 cm^{-1} refers to the stretching vibration of $-NH_3^+$ in (*R*-/*S*-NEA)$_2CuCl_4$. The strong sharp peaks at 1600, 1500 and 750 cm^{-1} verify the presence of a naphthyl ring (Fig. S5a†). In Fig. S5b,† the stretching vibration of $-NH_3^+$ in (*R*-/*S*-CYHEA)$_6Cu_3Cl_{12}$ is located at 3000–3250 cm^{-1}, and the peak at 2900 cm^{-1} represents the C–H stretching vibration. The peak at around 1599 cm^{-1} is attributed to the N–H stretching.[37] As shown in the Raman spectra (Fig. S5c and d†), the peaks in the range of 50–300 cm^{-1} are considered to be Cu–Cl bonds. C–H symmetric bending and asymmetric bending are observed at around 1400 cm^{-1} and its stretching is located at around 3000 cm^{-1}. N–H symmetric bending and asymmetric bending are observed near 1400 cm^{-1} and its stretching is

observed at around 3170 cm^{-1}. For (*R*-/*S*-NEA)$_2$CuCl$_4$, the vibration mode of Cu–Cl appears at 74, 174, 219 and 275 cm^{-1}, and those of (*R*-/*S*-CYHEA)$_6$Cu$_3$Cl$_{12}$ locate at 72 cm^{-1} and the wide peak is located at around 275 cm^{-1}. It is consistent with the literature.[38–40]

We also studied the morphology and microstructures of the chiral thin films by scanning electron microscopy (SEM). From the digital photos (Fig. S6a and d†), we could find that (*R*-NEA)$_2$CuCl$_4$ and (*R*-CYHEA)$_6$Cu$_3$Cl$_{12}$ uniformly grow on the substrate. The (*R*-NEA)$_2$CuCl$_4$ and (*R*-CYHEA)$_6$Cu$_3$Cl$_{12}$ thin films exhibited uniform distribution in the SEM image (Fig. S6b, c, e and f†). Homogeneous striped folds could be seen on the (*R*-NEA)$_2$CuCl$_4$ thin film. But there were cracks on the surface of the (*R*-CYHEA)$_6$Cu$_3$Cl$_{12}$ thin film. The fabrication of a perovskite thin film is a recrystallization process including nucleation and crystal growth. The number of nucleation sites and the crystal growth rate determine the quality of the film.[41] We speculate that the more nucleation sites and lower crystal growth rate of (*R*-NEA)$_2$CuCl$_4$ made it smoother than the (*R*-CYHEA)$_6$Cu$_3$Cl$_{12}$ thin film. The smooth morphology of (*R*-NEA)$_2$CuCl$_4$ is a benefit for a high SHG coefficient while the (*R*-CYHEA)$_6$Cu$_3$Cl$_{12}$ film with cracks blocks a small part of the incident light and generated light, contributing to lower SHG properties.

Surprisingly, we first find that (*R*-/*S*-NEA)$_2$CuCl$_4$ and (*R*-/*S*-CYHEA)$_6$Cu$_3$Cl$_{12}$ exhibit magnetic properties. In Fig. 2a and b, the magnetic moment of (*R*-/*S*-NEA)$_2$CuCl$_4$ is approximately two times as large as that of (*R*-/*S*-CYHEA)$_6$Cu$_3$Cl$_{12}$ at 2 K, which can be attributed to different ligand–metal charge transfer processes.[24,34] On one hand, Cu^{2+} and Cl^- can form a hybrid orbital near the Fermi level and generate $[CuCl_4]^{2-}$ or $[Cu_3Cl_{10}]^{4-}$ on the basis of ionic polarization theory. On the other hand, the electron density and ion size affect the process of ligand-to-metal charge transfer. The electron donating capacity of the alkyl ring is better than that of the benzene ring, and $[Cu_3Cl_{10}]^{4-}$ is larger than $[CuCl_4]^{2-}$. Therefore, the ligand-to-metal charge transfer in (*R*-/*S*-CYHEA)$_6$Cu$_3$Cl$_{12}$ is stronger than that in (*R*-/*S*-NEA)$_2$CuCl$_4$, so that Cu d^9 in (*R*-/*S*-CYHEA)$_6$Cu$_3$Cl$_{12}$ is close to d^{10}, and its magnetic moment is weaker. Magnetization decreases when the temperature varied from 2 to 30 K, and magnetic field-dependent magnetization showed a linear relationship, indicating that (*R*-/*S*-NEA)$_2$CuCl$_4$ and (*R*-/*S*-CYHEA)$_6$Cu$_3$Cl$_{12}$ are paramagnetic materials. Different from 2D corner-sharing perovskites, whose continuous metal-halogen bonds provide a path for electron transfer, the isolated Cu–Cl units in (*R*-/*S*-NEA)$_2$CuCl$_4$ and (*R*-/*S*-CYHEA)$_6$Cu$_3$Cl$_{12}$ only possess weak interactions.

To facilitate the subsequent testing, we fabricated a thin film by spin-coating the perovskite precursor on quartz substrates and evaporating the solvent at room temperature in air. As shown in Fig. S7,† the XRD patterns of (*R*-NEA)$_2$CuCl$_4$ and (*R*-CYHEA)$_6$Cu$_3$Cl$_{12}$ thin films are identical to that of the single crystals. (*R*-NEA)$_2$CuCl$_4$ thin films show sharp diffraction peaks at 6.36°, 12.68° and 19.04°, and those of the (*R*-CYHEA)$_6$Cu$_3$Cl$_{12}$ thin film are located at 6.80°, 9.70°, 13.58° and 22.22°. For (*R*-NEA)$_2$CuCl$_4$ and (*R*-CYHEA)$_6$Cu$_3$Cl$_{12}$ SCs, there are more diffraction peaks than the films due to the selectivity of lattice orientation during crystallization.

The UV-Vis absorption and CD spectra of (*R*-/*S*-NEA)$_2$CuCl$_4$ and (*R*-/*S*-CYHEA)$_6$Cu$_3$Cl$_{12}$ thin films are shown in Fig. 3. The UV-Vis absorption spectra extend from the ultraviolet to visible region. The CD spectra exhibit a strong response at the position corresponding to absorption. In Fig. 3a, (*R*-NEA)$_2$CuCl$_4$ thin films show obvious CD signals at 244 nm, 292 nm and 400 nm. The opposite CD signals are observed for (*S*-NEA)$_2$CuCl$_4$, indicating a preferential absorption of incident CPL. These peaks are identified to belong to the $\pi \rightarrow \pi^*$ transition of the naphthyl ring in the NEA molecule (244 nm and 292 nm) and ligand-to-metal charge transfer (400 nm). The maximum $|g_{CD}|$ is 0.0284 (Fig. 3b), which could be comparable

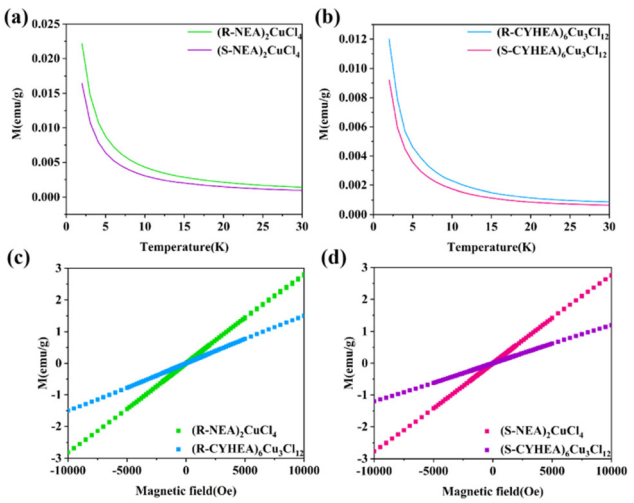

Fig. 2 Temperature-dependent magnetization of (a) (*R*-/*S*-NEA)$_2$CuCl$_4$ and (b) (*R*-/*S*-CYHEA)$_6$Cu$_3$Cl$_{12}$. Magnetic field-dependent magnetization of (c) R-type and (d) S-type perovskites.

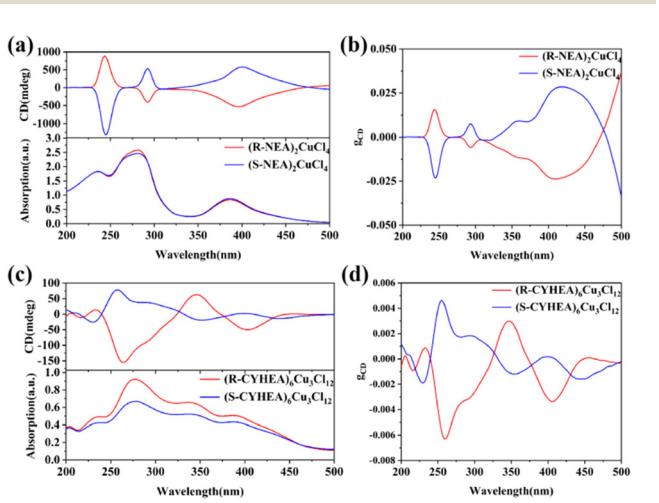

Fig. 3 The CD spectra of (a) (*R*-/*S*-NEA)$_2$CuCl$_4$ and (c) (*R*-/*S*-CYHEA)$_6$Cu$_3$Cl$_{12}$. The g_{CD} values of (b) (*R*-/*S*-NEA)$_2$CuCl$_4$ and (d) (*R*-/*S*-CYHEA)$_6$Cu$_3$Cl$_{12}$.

to other chiral perovskites.[18,42] When the chiral NEA molecule is replaced by CYHEA, the pattern of the CD signal shows a remarkable change. The mirror CD signals are located at 233 nm, 258 nm, 346 nm and 402 nm, and the maximum $|g_{CD}|$ is 0.0063 (Fig. 3c and d). Compared to $(R\text{-NEA})_2CuCl_4$, the peaks of $(R\text{-/}S\text{-CYHEA})_6Cu_3Cl_{12}$ at 233 and 258 nm are blue-shifted. This is because there is no conjugate structure in the CYHEA molecule. The red-shifted peak of ligand-to-metal charge transfer (402 nm) and the mirror signal at 300–350 nm are related to $[Cu_3Cl_{10}]^{4-}$. The mirror CD signals of $(R\text{-/}S\text{-NEA})_2CuCl_4$ and $(R\text{-/}S\text{-CYHEA})_6Cu_3Cl_{12}$ indicate that the chirality of organic cations has been successfully transferred to the whole structure, endowing these perovskites with intrinsic chirality. The mechanism for the chiroptical properties of the single crystals is ascribed to the interaction between chiral organic cations and achiral $[CuCl_4]^{2-}$ or $[Cu_3Cl_{10}]^{4-}$ inorganic units. According to a previous report, g_{CD} is related to the joint DOS.[11] Cu 3d, Cl 3p and the chiral amine (NEA or CYHEA) hybridize to make up the joint DOS. The larger the joint DOS, the higher g_{CD}. Moreover, the chiroptical properties are related to the magnetic transition dipole of HOIPs. The distance between adjacent inorganic layers and the interaction between organic cations and the inorganic units have an effect on the magnetic dipole moment of 2D HOIPs.[21] Here, the bond lengths of $(R\text{-NEA})_2CuCl_4$ vary from 2.2367 to 2.2605 Å, shorter than that of $(R\text{-CYHEA})_6Cu_3Cl_{12}$, which changes from 2.246 to 2.747 Å. We considered that the distance of $[CuCl_4]^{2-}$ in $(R\text{-NEA})_2CuCl_4$ is shorter than that of $[Cu_3Cl_{10}]^{4-}$ in $(R\text{-CYHEA})_6Cu_3Cl_{12}$; therefore its $|g_{CD}|$ is higher than that of $(R\text{-/}S\text{-CYHEA})_6Cu_3Cl_{12}$.

To reveal the mechanism why the Cu-based HIOPs have excellent chiral properties in this work, we calculated the partial density of states (DOS) of R-type enantiomers based on density functional theory (DFT). The generalized gradient approximation method with the Perdew–Burke–Ernzerhof (PBE) function was employed to describe the interaction between the core and electrons. An energy cutoff of 450 eV was used for the planewave expansion of the electronic wave function. The force and energy convergence criteria were set to 0.03 eV $Å^{-1}$ and 10^{-5} eV, respectively. As shown in Fig. 4, the bandgap of $(R\text{-NEA})_2CuCl_4$ and $(R\text{-/}S\text{-CYHEA})_6Cu_3Cl_{12}$ was determined to be 2.0 eV and 2.17 eV, smaller than the experimental values, 2.23 eV and 2.29 eV (the Tauc plots are provided in Fig. S8†), which is due to the discontinuity of the exchange–correlation function.[43] From Fig. 4c and d, we conclude that Cu 3d and Cl 3p orbitals contribute to the DOS of $(R\text{-NEA})_2CuCl_4$ and $(R\text{-/}S\text{-CYHEA})_6Cu_3Cl_{12}$ near the Fermi level and 3 eV, indicating that these bands are confined in $[CuCl_4]^{2-}$ and $[Cu_3Cl_{10}]^{4-}$ structures,[44] respectively. The conduction band is primarily originated from chiral amines *R*-NEA and *R*-CYHEA. In $(R\text{-NEA})_2CuCl_4$, the electrons transfer between *R*-NEA and $[CuCl_4]^{2-}$, leading to the chirality of the whole structure. $(R\text{-CYHEA})_6Cu_3Cl_{12}$ is similar to $(R\text{-NEA})_2CuCl_4$.

Chiral amines break the centrosymmetric structures of the perovskites that endow the perovskites with NLO properties. As shown in Fig. S9,† we used a home-built device equipped with

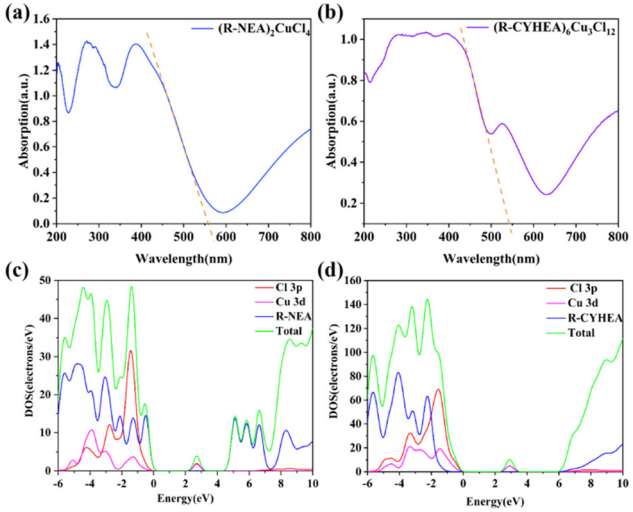

Fig. 4 The UV-Vis spectrum of (a) $(R\text{-NEA})_2CuCl_4$ and (b) $(R\text{-CYHEA})_6Cu_3Cl_{12}$ single crystals. The DOS of (c) $(R\text{-NEA})_2CuCl_4$ and (d) $(R\text{-CYHEA})_6Cu_3Cl_{12}$.

a femtosecond pulsed laser to study the SHG responses of $(R\text{-NEA})_2CuCl_4$ and $(R\text{-CYHEA})_6Cu_3Cl_{12}$ thin films and analyzed the second-order NLO effects of the Cu-based halide perovskites with different chiral amines. The band edge of both films is nearly 500 nm. Therefore, the wavelength-dependent SHG spectra of $(R\text{-NEA})_2CuCl_4$ and $(R\text{-CYHEA})_6Cu_3Cl_{12}$ thin films were recorded from 800 to 1040 nm with 20 nm step length and 50-mW pumping power at room temperature (Fig. 5a and b). Obvious SHG signals could be detected in $(R\text{-NEA})_2CuCl_4$ and $(R\text{-CYHEA})_6Cu_3Cl_{12}$ thin films within the excitation wavelength range of 820–1040 nm, while the detected SHG signals

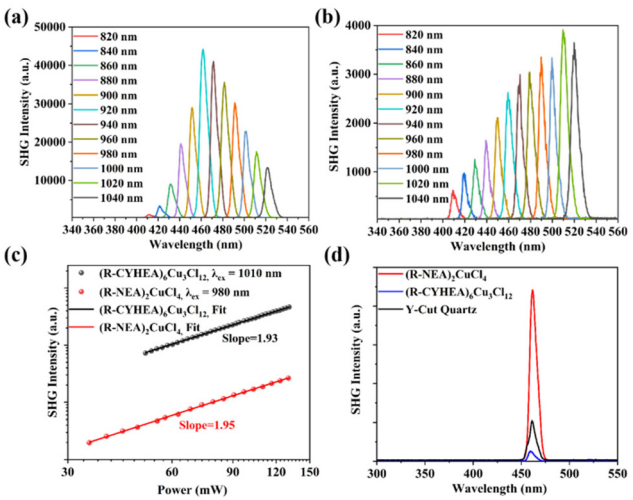

Fig. 5 The wavelength-dependent SHG response of (a) $(R\text{-NEA})_2CuCl_4$ and (b) $(R\text{-CYHEA})_6Cu_3Cl_{12}$ thin films. (c) The pumping power-dependent SHG response of $(R\text{-NEA})_2CuCl_4$ and $(R\text{-CYHEA})_6Cu_3Cl_{12}$ thin films. (d) The comparison of the SHG intensity between $(R\text{-NEA})_2CuCl_4$ and $(R\text{-CYHEA})_6Cu_3Cl_{12}$ thin films and Y-cut quartz under 920 nm excitation.

of the $(R\text{-CYHEA})_6Cu_3Cl_{12}$ thin film are lower than those of the $(R\text{-NEA})_2CuCl_4$ thin film. The position of SHG peaks locates at half of the pumped wavelength. As shown in Fig. 5c, SHG intensities show a linear relationship in logarithmic coordinates with the pumping power under 980 nm excitation of the $(R\text{-NEA})_2CuCl_4$ thin films and under 1010 nm excitation of the $(R\text{-CYHEA})_6Cu_3Cl_{12}$ thin films, respectively. The slope of the pumping power-dependent SHG intensities is approximately 2.0 for both the thin films, indicating the two-photon nature with different frequencies of a second-order NLO response. In Fig. S11(a),† we can conclude that the SHG intensity begins to drop when the incidence power is higher than 140 mW. Therefore, the laser damage threshold of $(R\text{-NEA})_2CuCl_4$ was about 0.56 mJ cm^{-2}. Similarly, the laser damage threshold of $(R\text{-CYHEA})_6Cu_3Cl_{12}$ was found to be 0.52 mJ cm^{-2} (Fig. S11(b)†). In order to compare the SHG intensities of $(R\text{-NEA})_2CuCl_4$ and $(R\text{-CYHEA})_6Cu_3Cl_{12}$ thin films directly, we tested the $(R\text{-NEA})_2CuCl_4$ and $(R\text{-CYHEA})_6Cu_3Cl_{12}$ thin films, as well as Y-cut quartz as a reference, under the same experimental conditions (Fig. S10†). Fig. 5d shows the SHG response intensities of $(R\text{-NEA})_2CuCl_4$ and $(R\text{-CYHEA})_6Cu_3Cl_{12}$ thin films and Y-cut quartz at 460 nm. Furthermore, we found that the second-order NLO coefficients (d_{eff}) of $(R\text{-NEA})_2CuCl_4$ and $(R\text{-CYHEA})_6Cu_3Cl_{12}$ thin films were 11.74 and 3.04 pm V^{-1}, respectively, and the d_{eff} of $(R\text{-NEA})_2CuCl_4$ is more than 19 times larger than that of Y-cut quartz under 920 nm linearly polarized light.

The above data show that the SHG response of the $(R\text{-NEA})_2CuCl_4$ thin film is approximately 4 times as large as that of the $(R\text{-CYHEA})_6Cu_3Cl_{12}$ thin film, indicating that the chiral amine has a remarkable influence. The detectable SHG response in the $(R\text{-CYHEA})_6Cu_3Cl_{12}$ thin films may be ascribed to the increased asymmetry of the thin films. We speculate that the amino groups of the naphthylethylamine molecule formed n–π* conjugation with the aromatic ring, which made the interactions between N–H and Cl stronger, and its planar structure endowed $(R\text{-NEA})_2CuCl_4$ with greater asymmetry. So its NLO activity is much stronger. Compared to flexible non-aromatic amines, the structure of naphthylethylamine is more stable. It is possible that its planar structure causes the chiral amines to arrange regularly and leads to more severe symmetry breaking. In contrast, the flexible cyclohexylethylamine is more likely to cause structural transformation and more complex intermolecular interactions. Thus, $(R\text{-}/S\text{-CYHEA})_6Cu_3Cl_{12}$ is prone to smaller symmetry breaking, and the SHG activity is significantly different in $(R\text{-NEA})_2CuCl_4$ and $(R\text{-CYHEA})_6Cu_3Cl_{12}$.[25] This work provides insight into NLO properties for chiral HOIPs, demonstrating that chiral Cu-based HOIPs have great potential in NLO applications.

Conclusion

In this work, we first synthesized $(R\text{-}/S\text{-NEA})_2CuCl_4$ and $(R\text{-}/S\text{-CYHEA})_6Cu_3Cl_{12}$ bulk single crystals *via* a slow solvent evaporation method. Each pair of chiral perovskite enantiomers showed mirror CD signals. Importantly, an obvious SHG response could be detected in the $(R\text{-NEA})_2CuCl_4$ and $(R\text{-CYHEA})_6Cu_3Cl_{12}$ thin films. The second-order NLO coefficient of the $(R\text{-NEA})_2CuCl_4$ thin films was approximately 4 times as large as that of the $(R\text{-CYHEA})_6Cu_3Cl_{12}$ thin films. Furthermore, the XRD patterns showed no change after exposure to air for 6 months and the Cu element is more environmentally friendly than toxic Pb. Our work demonstrates that chiral Cu-based HOIPs are potential materials for NLO devices

Conflicts of interest

There are no conflicts to declare.

Acknowledgements

This work was supported by the National Natural Science Foundation of China under No. 21909161, 22278315 and 52172045.

References

1 A. Autere, H. Jussila, Y. Dai, Y. Wang, H. Lipsanen and Z. Sun, *Adv. Mater.*, 2018, **30**, 1705963.
2 L. Zhao, X. Han, Y. Zheng, M.-H. Yu and J. Xu, *Adv. Photo. Res.*, 2021, **2**, 2100056.
3 J. Xu, S. Semin, D. Niedzialek, P. H. J. Kouwer, E. Fron, E. Coutino, M. Savoini, Y. Li, J. Hofkens, H. Uji-I, D. Beljonne, T. Rasing and A. E. Rowan, *Adv. Mater.*, 2013, **25**, 2084–2089.
4 Y. Rong, S. Venkatesan, R. Guo, Y. Wang, J. Bao, W. Li, Z. Fan and Y. Yao, *Nanoscale*, 2016, **8**, 12892–12899.
5 J. Zhou, Y. Liu, H. Wu, H. Yu, Z. Lin, Z. Hu, J. Wang and Y. Wu, *Angew. Chem., Int. Ed.*, 2020, **59**, 19006–19010.
6 Z. Lin, Y. Zhang, M. Gao, J. A. Steele, S. Louisia, S. Yu, L. N. Quan, C.-K. Lin, D. T. Limmer and P. Yang, *Matter*, 2021, **4**, 2392–2402.
7 D. G. Billing and A. Lemmerer, *Acta Crystallogr., Sect. E: Struct. Rep. Online*, 2003, **59**, m381–m383.
8 Y. Zheng, J. Xu and X. H. Bu, *Adv. Opt. Mater.*, 2022, **10**, 2101545.
9 J. Ahn, S. Ma, J. Y. Kim, J. Kyhm, W. Yang, J. A. Lim, N. A. Kotov and J. Moon, *J. Am. Chem. Soc.*, 2020, **142**, 4206–4212.
10 C. Zhou, Y. Chu, L. Ma, Y. Zhong, C. Wang, Y. Liu, H. Zhang, B. Wang, X. Feng, X. Yu, X. Zhang, Y. Sun, X. Li and G. Zhao, *Phys. Chem. Chem. Phys.*, 2020, **22**, 17299–17305.
11 Z. Guo, J. Li, C. Wang, R. Liu, J. Liang, Y. Gao, J. Cheng, W. Zhang, X. Zhu, R. Pan and T. He, *Angew. Chem., Int. Ed.*, 2021, **60**, 8441–8445.
12 P. J. Huang, K. Taniguchi and H. Miyasaka, *J. Am. Chem. Soc.*, 2019, **141**, 14520–14523.
13 P. J. Huang, K. Taniguchi, M. Shigefuji, T. Kobayashi and H. Miyasaka, *Adv. Mater.*, 2021, **33**, 2008611.

14 Z. Guo, J. Li, R. Chen and T. He, *Prog. Quantum Electron.*, 2022, **82**, 100375.
15 J. Wang, C. Fang, J. Ma, S. Wang, L. Jin, W. Li and D. Li, *ACS Nano*, 2019, **13**, 9473–9481.
16 J. Ma, C. Fang, C. Chen, L. Jin, J. Wang, S. Wang, J. Tang and D. Li, *ACS Nano*, 2019, **13**, 3659–3665.
17 L. Wang, Y. Xue, M. Cui, Y. Huang, H. Xu, C. Qin, J. Yang, H. Dai and M. Yuan, *Angew. Chem., Int. Ed.*, 2020, **59**, 6442–6450.
18 A. Ishii and T. Miyasaka, *Sci. Adv.*, 2020, **6**, eabd3274.
19 Z. Liu, C. Zhang, X. Liu, A. Ren, Z. Zhou, C. Qiao, Y. Guan, Y. Fan, F. Hu and Y. S. Zhao, *Adv. Sci.*, 2021, **8**, 2102065.
20 J. X. Gao, W. Y. Zhang, Z. G. Wu, Y. X. Zheng and D. W. Fu, *J. Am. Chem. Soc.*, 2020, **142**, 4756–4761.
21 J. T. Lin, D. G. Chen, L. S. Yang, T. C. Lin, Y. H. Liu, Y. C. Chao, P. T. Chou and C. W. Chiu, *Angew. Chem., Int. Ed.*, 2021, **60**, 21434–21440.
22 H. Lu, J. Wang, C. Xiao, X. Pan and Z. V. Vardeny, *Sci. Adv.*, 2019, **5**, eaay0571.
23 H. Lu, C. Xiao, R. Song, T. Li, A. E. Maughan, A. Levin, R. Brunecky, J. J. Berry, D. B. Mitzi, V. Blum and M. C. Beard, *J. Am. Chem. Soc.*, 2020, **142**, 13030–13040.
24 Y. Lu, Q. Wang, R. He, F. Zhou, X. Yang, D. Wang, H. Cao, W. He, F. Pan, Z. Yang and C. Song, *Angew. Chem., Int. Ed.*, 2021, **60**, 23578–23583.
25 Y. Hu, F. Florio, Z. Chen, W. A. Phelan, M. A. Siegler, Z. Zhou, Y. Guo, R. Hawks, J. Jiang, J. Feng, L. Zhang, B. Wang, Y. Wang, D. Gall, E. F. Palermo, Z. Lu, X. Sun, T.-M. Lu, H. Zhou, Y. Ren, E. Wertz, R. Sundararaman and J. Shi, *Sci. Adv.*, 2020, **6**, eaay4213.
26 C. Yuan, X. Li, S. Semin, Y. Feng, T. Rasing and J. Xu, *Nano Lett.*, 2018, **18**, 5411–5417.
27 Y. L. Zeng, X. Q. Huang, C. R. Huang, H. Zhang, F. Wang and Z. X. Wang, *Angew. Chem., Int. Ed.*, 2021, **60**, 10730–10735.
28 C. K. Yang, W. N. Chen, Y. T. Ding, J. Wang, Y. Rao, W. Q. Liao, Y. Y. Tang, P. F. Li, Z. X. Wang and R. G. Xiong, *Adv. Mater.*, 2019, **31**, 1808088.
29 L. Yao, Z. Zeng, C. Cai, P. Xu, H. Gu, L. Gao, J. Han, X. Zhang, X. Wang, X. Wang, A. Pan, J. Wang, W. Liang, S. Liu, C. Chen and J. Tang, *J. Am. Chem. Soc.*, 2021, **143**, 16095–16104.
30 J. Zhao, Y. Zhao, Y. Guo, X. Zhan, J. Feng, Y. Geng, M. Yuan, X. Fan, H. Gao, L. Jiang, Y. Yan and Y. Wu, *Adv. Funct. Mater.*, 2021, **31**, 2105855.
31 Z. Huang, B. P. Bloom, X. Ni, Z. N. Georgieva, M. Marciesky, E. Vetter, F. Liu, D. H. Waldeck and D. Sun, *ACS Nano*, 2020, **14**, 10370–10375.
32 D. Fu, J. Xin, Y. He, S. Wu, X. Zhang, X.-M. Zhang and J. Luo, *Angew. Chem., Int. Ed.*, 2021, **60**, 20021–20026.
33 H. M. Mande, P. S. Ghalsasi and A. Navamoney, *Polyhedron*, 2015, **91**, 141–149.
34 B. Sun, X. F. Liu, X. Y. Li, Y. Zhang, X. Shao, D. Yang and H. L. Zhang, *Chem. Mater.*, 2020, **32**, 8914–8920.
35 Z. Guo, J. Li, J. Liang, C. Wang, X. Zhu and T. He, *Nano Lett.*, 2022, **22**, 846–852.
36 S. Liu, L. He, Y. Wang, P. Shi and Q. Ye, *Chin. Chem. Lett.*, 2022, **33**, 1032–1036.
37 K. Patel and A. Patel, *Inorg. Chim. Acta*, 2012, **382**, 79–83.
38 H. Zhao, H. Fu, Z. Hu, Q. Fu, H. Tao, J. Weng, L. Xiong and Z. Cheng, *CrystEngComm*, 2021, **23**, 5208–5213.
39 B. G. H. M. Groeneveld, H. Duim, S. Kahmann, O. De Luca, E. K. Tekelenburg, M. E. Kamminga, L. Protesescu, G. Portale, G. R. Blake, P. Rudolf and M. A. Loi, *J. Mater. Chem. C*, 2020, **8**, 15377–15384.
40 A. Elattar, H. Suzuki, R. Mishima, K. Nakao, H. Ota, T. Nishikawa, H. Inoue, A. K. K. Kyaw and Y. Hayashi, *J. Mater. Chem. C*, 2021, **9**, 3264–3270.
41 X. Liu, K. Yan, D. Tan, X. Liang, H. Zhang and W. Huang, *ACS Energy Lett.*, 2018, **3**, 2701–2707.
42 C. Chen, L. Gao, W. Gao, C. Ge, X. Du, Z. Li, Y. Yang, G. Niu and J. Tang, *Nat. Commun.*, 2019, **10**, 1927.
43 M. Yang, H. Cheng, Y. Xu, M. Li and Y. Ai, *Chin. Chem. Lett.*, 2022, **33**, 2143–2146.
44 C. Zhou, H. Lin, H. Shi, Y. Tian, C. Pak, M. Shatruk, Y. Zhou, P. Djurovich, M.-H. Du and B. Ma, *Angew. Chem., Int. Ed.*, 2018, **57**, 1021–1024.